# Pulsed laser deposition, characterization and thermochemical stability of SrFeyCo1-yOx thin films

Tunney, Jim; Whitfield, Pamela; Du, Xiaomei; Post, Michael



**Publisher's version / Version de l'éditeur:**
http://dx.doi.org/10.1016/S0040-6090(03)00010-5
*Thin Solid Films, 426, 1, pp. 221-231, 2003*

Available online at www.sciencedirect.com
SCIENCE DIRECT®
Thin Solid Films 426 (2003) 221–231
thin solid films
www.elsevier.com/locate/tsf

# Pulsed laser deposition, characterization and thermochemical stability of $SrFe_yCo_{1-y}O_x$ thin films

James J. Tunney*, Pamela Whitfield, Xiaomei Du, Michael L. Post

*Institute for Chemical Process and Environmental Technology, National Research Council of Canada, Montreal Road, Ottowa, Ontario, Canada K1A 0R6*

Received 19 January 2002; received in revised form 22 October 2002; accepted 17 December 2002

**Abstract**

$SrFe_yCo_{1-y}O_x$ ($y=0.0$, 0.25, 0.50, 0.75, 0.90 and 1.0) thin films on sapphire substrates were prepared by laser deposition, and characterized by elemental analysis using Rutherford backscattering spectroscopy, particle-induced X-ray emission and inductively coupled plasma-atomic emission spectroscopy, X-ray photoelectron spectroscopy, X-ray diffraction and scanning electron microscopy. In order to determine the relative stability of the films at 500 °C, the films were subjected to both thermochemical oxidizing and reducing treatments in 100% $O_2$ and 2% $H_2$/argon gas mixtures, respectively. Thermochemical oxidizing treatments of the $SrFe_yCo_{1-y}O_x$ films resulted in dark-colored oxygen-rich films. Thermochemical reduction resulted in transparent yellow–brown films for the more iron-rich films, but not for the Co-rich films, which remained dark-colored. Fe-rich $SrFe_yCo_{1-y}O_x$ ($y=$ 0.50, 0.75 and 1.0) films exhibited the greatest degree of structural variation, resulting from the cubic perovskite → brownmillerite phase change upon reduction. Films with higher Co substitution showed smaller variations in the unit cell parameters. The $SrCoO_x$ film was unstable under reducing conditions, with a Sr-enriched carbonate layer forming at the interface after exposure to ambient atmosphere. XRD measurements conducted in situ at 500 °C in both air and nitrogen gases confirmed that reversible structural changes occur in the film solely as a consequence of changing the surrounding gas composition, with the largest changes in lattice spacing occurring for the $SrFe_{0.75}Co_{0.25}O_x$ and $SrFe_{0.5}Co_{0.5}O_x$ films.


*Keywords:* Laser ablation; Sensors; Phase transitions; X-Ray diffraction

## 1. Introduction

Perovskite-type materials based on the composition $SrFe_yCo_{1-y}O_x$ have been shown to exhibit both fast oxide ionic conductivity and good electronic conductivity [1–3]. This makes them suitable candidates for applications such as solid oxide fuel cell cathodes, oxygen membranes and sensor materials. For sensor applications, the materials should be in either the thin or thick film state. It has been demonstrated that thin films of these types of materials may be grown by pulsed laser deposition (PLD) [4–10]. Depending on the deposition conditions, PLD can yield both dense and porous films with metal stoichiometry equal to that of the target material.

In a previous study it was shown that $SrFe_yCo_{1-y}O_x$ thin films grown by PLD onto sapphire substrates exhibit promising gas sensor functionality [4]. The cubic perovskite (CP)–brownmillerite (BM) phase transition for some of these films was attributed to enhanced gas sensitivity. The conditions of temperature and gas composition at which this phase transition occurs could be controlled by choosing the appropriate degree of iron and cobalt substitution in the $SrFe_yCo_{1-y}O_x$ structure. It was also shown that some of these films exhibited a degree of temperature independence for the resistance response, while maintaining good gas sensitivity. This material property is important when trying to minimize the influence of unstable temperatures on the performance of a gas-sensing device. The present study focuses on the preparation and characterization of these films, and their thermochemical stability under reducing and oxidizing environments.

*Corresponding author. Fax: +1-613-991-2384.

0040-6090/03/$ - see front matter 
doi:10.1016/S0040-6090(03)00010-5

## 2. Experimental

### 2.1. Target preparation

Pellets of different $SrFe_yCo_{1-y}O_x$ compositions ($y$= 0, 0.25, 0.5, 0.75, 0.9 and 1.0) were prepared by conventional ceramic preparation techniques. $SrCO_3$, $Fe_2O_3$ and $Co_3O_4$ powders ( 99.99% pure on a metal basis) were mixed and ground together in the required quantities, followed by heat treatment at 1100 °C under either an argon or oxygen atmosphere. The samples were ground up again and the resulting black or brown powders were characterized by XRD. At this point, if the product was not single phase as evidenced by XRD, the product was further heated in oxygen, ground up and again examined by XRD. Once the single-phase product was obtained in the powdered form, the powder was pelletized and sintered at 1150 °C in oxygen. After XRD analysis confirmed the pellet to be single phase, the pellet could be used as the target material for the deposition of $SrFe_yCo_{1-y}O_x$ films by pulsed laser deposition.

### 2.2. Film deposition

Preparation of 250–350-nm thin films of composition $SrFe_yCo_{1-y}O_x$ ($y$=0, 0.25, 0.5, 0.75, 0.9 and 1.0) was carried out by PLD using a Lambda Physik LPX305i, $\lambda$=248 nm KrF excimer laser at an energy of 600 mJ/pulse (fluence 1.5 J/cm$^2$) and a frequency of 8 Hz. The substrate was (1102) single-crystal sapphire mounted onto an alumina heater allowing for deposition temperatures up to 800 °C. The films were deposited for 20 min under a background oxygen pressure of 100 mtorr, followed by cooling at approximately 10 °C/min in a background oxygen pressure of 400 torr. XRD analysis was performed on all PLD targets, both before and after deposition, in order to confirm that decomposition of the target material did not occur as a consequence of repeated laser exposure. Thickness determination was performed using a Dektak IIA stylus profiler after shadow-masking portions of the films.

### 2.3. Thermochemical treatments

The thermochemical stability of the films was tested under two separate environments, designed to simulate the operation of these materials as thin-film gas sensors under both thermochemical reducing and oxidizing environments. The films were exposed to either flowing oxygen or to a 2% $H_2$/argon gas mixture ($O_2$ 1 ppm; $H_2O$ 3 ppm) at 500 °C in a tube furnace for 16 h, followed by cooling to room temperature at a rate of 1 °C/min. Typically, a 1-cm$^2$ $SrFe_yCo_{1-y}O_x$ film was cut into two pieces, with one piece being treated in oxygen and the other in 2% $H_2$/Argon.

### 2.4. XRD characterization

XRD characterization of the $SrFe_yCo_{1-y}O_x$ powders, targets and films at ambient temperatures was performed using a $CuK_\alpha$ Scintag XDS2000 Bragg–Brentano geometry diffractometer with a secondary-beam graphite monochromator. Powders were uniformly spread over a low-background Si holder, whereas pellets and films were placed on a low-background Si holder with the vertical displacement carefully adjusted with shims in order to minimize sample displacement errors.

### 2.5. SEM analysis

SEM analysis of the films was performed on a JEOL JSM 5300 instrument using a 20-kV electron beam. Additional high-resolution FEG-SEM images were performed on selected films using a Hitachi S-4700 instrument.

### 2.6. RBS/PIXE analysis

Rutherford backscattering (RBS) experiments were performed on $SrFe_yCo_{1-y}O_x$ films in a Tandetron system using He alpha particles accelerated to 2.0 MeV using a van der Graaf accelerator. The detector angle was 165°, the target angle was 7° and a solid angle of 10.205 msr was used for all measurements with total acquisitions of 1–2 μC. RBS simulations to estimate film stoichiometry were performed using the QUARK software program [11]. The RBS spectra for Co and Fe could not be resolved with RBS, but were instead determined by proton-induced X-ray emission (PIXE) analysis using protons accelerated to 1.5 MeV for a total acquisition of 2.0 μC.

### 2.7. ICP-AES analysis

Additional elemental analysis of the films was performed by inductively coupled plasma-atomic emission spectroscopy (ICP-AES) using a Perkin Elmer Optima 3000 RV. The films were first completely dissolved in excess nitric acid before analysis and the resulting solutions analyzed using calibrated solutions for the following spectral lines: Sr, 421.522 nm; Fe, 259.940 nm; and Co, 230.786 nm.

### 2.8. XPS analysis

X-Ray photoelectron spectroscopy (XPS) was performed on a Kratos Axis instrument using monochromated $AlK_\alpha$ radiation (1486.6 eV) using an acceptance

Table 1
Physical and chemical properties of the $SrFe_yCo_{1-y}O_x$ series of films

| Target composition | Film thickness (nm) | Phase | Orientation | Film morphology | | Bulk film composition | | Film color | |
|---|---|---|---|---|---|---|---|---|---|
| | | | | Cracks | Roughness | ICP-AES | RBS/PIXE | 100% $O_2$ | 2% $H_2$/Ar |
| $SrFeO_x$ | 300 | CP | (110) | Faint, 1–2 μm | 200 nm | $SrFe_{1.04}O_x$ | $SrFe_{1.06}O_x$ | Black | Transp. yellow |
| $SrFe_{0.9}Co_{0.1}O_x$ | 250 | CP | (110) | Faint, 1–2 μm | 200 nm | $SrFe_{0.95}Co_{0.12}O_x$ | – | Black | Transp. yellow |
| $SrFe_{0.75}Co_{0.25}O_x$ | 300 | CP | (110) | Smooth | 200 nm | $SrFe_{0.83}Co_{0.25}O_x$ | $SrFe_{0.75}Co_{0.26}O_x$ | Black | Brown–yellow |
| $SrFe_{0.5}Co_{0.5}O_x$ | 350 | CP | (200) | 1–10 μm | 200 nm | $SrFe_{0.53}Co_{0.58}O_x$ | $SrFe_{0.52}Co_{0.57}O_x$ | Black | Brown–black |
| $SrFe_{0.25}Co_{0.75}O_x$ | 350 | CP | (200) | Smooth | 200 nm | $SrFe_{0.27}Co_{0.82}O_x$ | $SrFe_{0.23}Co_{0.74}O_x$ | Black | Black |
| $SrCoO_x$ | 350 | Hex | (201) | 200-nm particles | | $SrCo_{1.04}O_x$ | $SrCo_{1.12}O_x$ | Black | Black |

CP, cubic perovskite lattice; Hex, hexagonal lattice determined for $SrCoO_x$. Preferential orientation of the film was determined by its most intense reflection.

angle of 8°, with the angle between the X-ray source and the detector being fixed at 65°. All samples were exposed to ambient atmosphere both before and after transfer to the spectrometer. An initial survey scan was taken to identify all elements present near the surface of the film. This was followed by a 15–30-s Ar sputter etch to pre-clean the surface, a second survey scan, and finally high-resolution spectra of the following XPS peaks: C 1s, O 1s, Sr 3d, Co 2p and Fe 2p. All peaks were referenced with respect to the amorphous carbon C 1s peak at binding energy of 285.0 eV. Atomic stoichiometries were calculated based on the integrated peak intensities of the high-resolution spectra after adjusting for differences in relative sensitivity factors, estimated from the Kratos software.

### 2.9. In situ high-temperature XRD studies

X-Ray diffraction measurements were made at 500 °C under air and nitrogen in an Anton-Parr HTK1200 furnace. The furnace was mounted on a $CuK_\alpha$ Brüker D8 diffractometer equipped for parallel-beam geometry with primary and secondary double Göbel mirrors [12]. The mirrors are very effective at removing $CuK_\beta$ radiation, so there is no interference from sapphire $K_\beta$ reflections. The parallel-beam geometry renders the system insensitive to sample displacement errors in both sample mounting and due to thermal expansion. The system was calibrated for peak position using the NIST SRM 660a $LaB_6$ standard. The films were heated to 500 °C at a rate of 6 °C/min and in ultra-high-purity (UHP) $N_2$ ($[O_2]$ 1 ppm; $[H_2O]$ 3 ppm), and allowed to equilibrate overnight. Once data collection was complete, the gas was switched to air, and the scan repeated once the film was left to equilibrate for approximately 1 h. UHP nitrogen was used rather than argon due to its weaker X-ray scattering. Lattice parameters were obtained from a full pattern using the Pawley method [13] with the TOPAS software package [14]. Peaks were fitted with a pseudo-Voigt profile function, together with a correction for axial divergence.

## 3. Results and discussion

### 3.1. Film deposition and characterization

A series of films was deposited by PLD from six different target compositions (Table 1). The X-ray diffraction patterns of the $SrFe_yCo_{1-y}O_x$ targets were measured both before and after laser deposition in order to confirm that decomposition of the bulk target material did not take place due to repeated laser pulses. It has previously been demonstrated that target decomposition during the course of the deposition process can lead to the formation of non-stoichiometric films [9].

For all target materials employed, very little target decomposition was observed by XRD. Fig. 1 shows this for both the $SrCoO_x$ and $SrFeO_x$ targets. In the case of $SrFeO_x$, the presence of a low-intensity peak next to the (110) cubic perovskite reflection at $2\Theta = 31.6°$ is attributed to decomposition of the cubic perovskite phase [15] with approximate composition $SrFeO_{2.9}$ to the oxygen-deficient $SrFeO_{2.5}$ brownmillerite phase [16]. In contrast, no significant change was observed for the $SrCoO_x$ target, despite the more complex phase relations for this system. $SrCoO_x$ could be indexed to either a hexagonal $SrCoO_{2.52}$ phase [17] that is structurally related to the oxygen-deficient 2H-$BaNiO_3$ or to a rhombohedral $Sr_2Co_2O_5$ structure (R) [18]. It has been demonstrated that as the high-temperature brownmillerite phase $SrCoO_{2.5}$ cools in air, phase separation into $SrCo_5O_{15}$ and $Co_3O_4$ occurs, with powder neutron diffraction identifying the $Sr_6Co_5O_{15}$ phase as rhombohedral and related to the 2H-hexagonal perovskite-type phase [19]. Despite some changes in bulk oxygen composition as evidenced by XRD, caused by the exposure to repeated laser ablation pulses, all the targets remained stoichiometric in terms of the Sr/M ratio (M = Co, Fe).

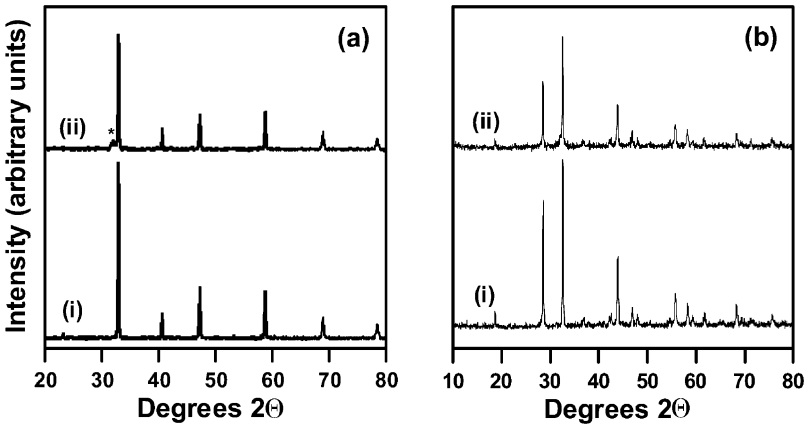


Fig. 1. XRD of (a) $SrFeO_x$ and (b) $SrCoO_x$ targets (i) before and (ii) after deposition. * indicates the presence of brownmillerite phase.

Under the deposition conditions employed, preferentially oriented polycrystalline films were obtained with thickness of between 250 and 350 nm. Stylus profiling also showed that the film thickness could vary through the 1–2-$cm^2$ surface of the film by as much as 10–20%. The as-deposited films appeared shiny black or dark brown. SEM analysis of the films showed varying morphology, from cracks to various degrees of graininess (Table 1). Three typical examples of film morphology are shown in Fig. 2. The morphology of all films except $SrCoO_x$ did not change as a result of the subsequent thermochemical oxidizing and reducing steps (Section 3.2).

The $SrFe_yCo_{1-y}O_x$ ($y=0.25$, 0.5, 0.9 and 1.0) films were all indexed to the cubic perovskite phase and were either preferentially (110)-oriented for $y=0.5$, 0.75, 0.9 and 1.0 or (200)-oriented for $y=0.25$ and 0.5. Depending on small variations in deposition conditions, such as the deposition temperature, $SrFe_{0.5}Co_{0.5}O_x$ could either adopt a (110) or a (200) preferential orientation. $SrCoO_x$ films exhibited (201) preferential orientation with respect to the hexagonal phase [17].

The bulk stoichiometry of the films was independently evaluated by both RBS-PIXE and ICP-AES and values were consistent to within 10% of the expected metal stoichiometry (Table 1). The oxygen stoichiometry of the films could not be determined using these techniques. The RBS and PIXE spectra for a $SrFe_{0.5}Co_{0.5}O_x$ film are shown in Fig. 3. Cobalt and iron could not be discriminated using RBS alone, so for films containing both Co and Fe, PIXE spectra were obtained. Some of the films showed evidence of variations in metal stoichiometry with film depth. This variation could be modeled with the QUARK software using either two or three layers with different Sr/M stoichiometry. The compositions shown in Table 1 are the overall stoichiometry as determined over the entire thickness of the films.

For the $SrFe_{0.5}Co_{0.5}O_x$ film (Fig. 3a), the simulation was modeled using two $SrFe_yCo_{1-y}O_x$ layers with differing stoichiometry. The layer closest to the surface was 63 nm thick with $Sr/M=0.78$, while the second was 290 nm thick with $Sr/M=0.95$. The reasons for the inhomogeneity in some of these films is not fully understood, but may be related to the formation of a surface segregated phase at the perovskite interface [20–22].

Deconvolution and integration of the Fe and Co $K_\alpha$ and $K_\beta$ X-ray peaks shown in the PIXE spectra in Fig. 3b, followed by adjusting for the relative sensitivity factors, yielded a Co/Fe ratio of 1.1 compared to an expected value of 1.0. Comparison of the bulk film stoichiometry obtained from RBS/PIXE and ICP-AES shows that the values are consistent to within 10%, with most films showing a slight Co+Fe enrichment with respect to Sr. It was estimated that the accuracy of the data obtained by both these techniques is 10%, so this apparent Co+Fe enrichment may not be significant.

### *3.2. Thermochemical stability of films*

The stability of the $SrFe_yCo_{1-y}O_x$ films at temperatures typical for gas sensor operation (500 °C) were investigated in both oxidizing (100% $O_2$) and reducing (2% $H_2$ in argon) environments (Section 2.3. All films exposed to oxygen at 500 °C remained black or black–brown, whereas some of the films exposed to 2% $H_2$ in argon turned yellow or yellow–brown. This change in color has previously been reported for $SrFeO_x$ films and is indicative of a change from the oxygen-rich cubic perovskite phase to the oxygen-deficient brownmillerite phase [23]. In particular, the iron-rich films, $SrFeO_x$, $SrFe_{0.9}Co_{0.1}O_x$ and $SrFe_{0.75}Co_{0.25}O_x$, all showed color changes to yellow or light brown as a result of the reducing treatment (Table 1).

The XRD patterns for the films also showed pronounced changes after the two different thermochemical

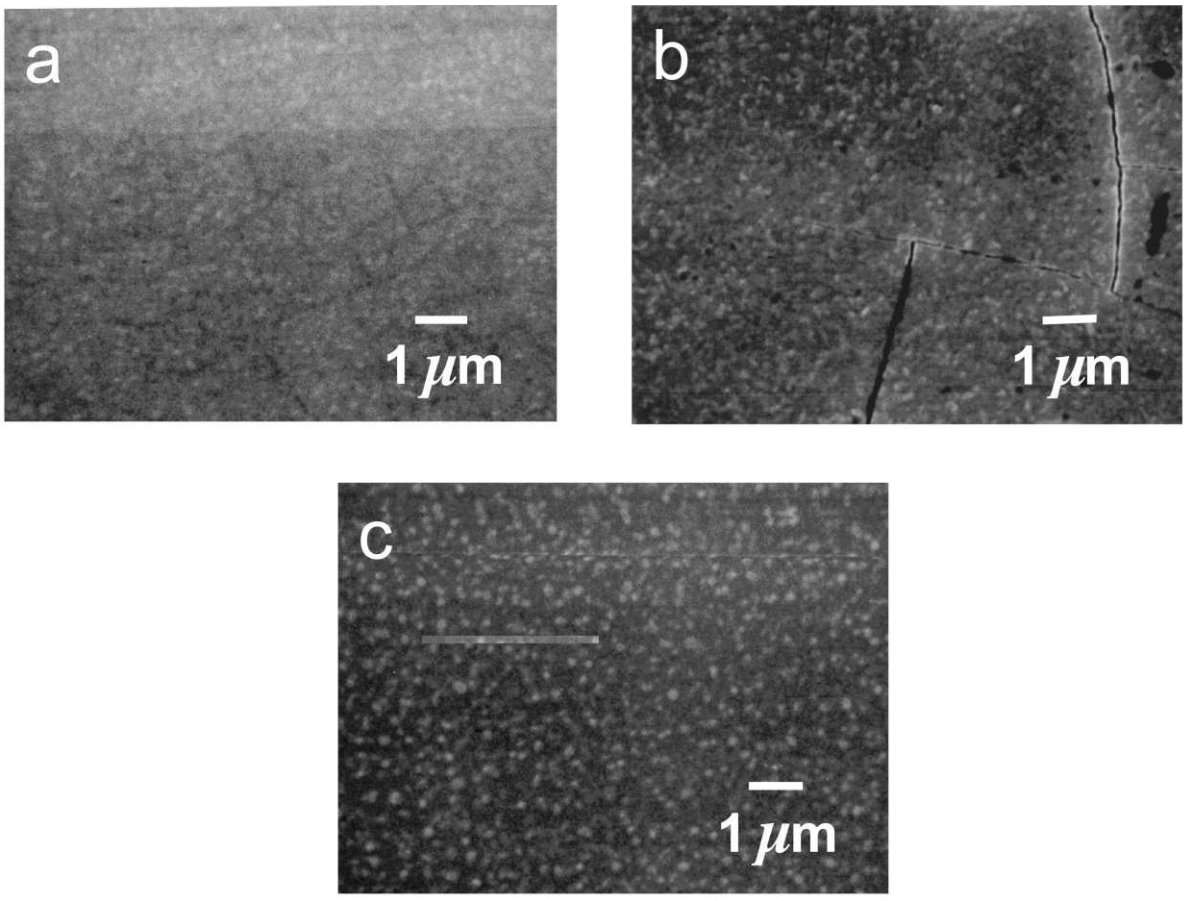


Fig. 2. SEM images of as-deposited films showing different types of film morphology: (a) $SrFeO_x$; (b) $SrFe_{0.50}Co_{0.50}O_x$; and (c) $SrCoO_x$.

treatments (Figs. 4 and 5). Thermal treatments in oxygen resulted in little structural change from the as-deposited films. The $SrFe_yCo_{1-y}O_x$ ($y=0.25$, 0.5, 075, 0.9 and 1.0) films were all indexed to the cubic perovskite phase, although the presence of a tetragonal perovskite phase should not be ruled out because of insufficient resolution [5,24]. The degree and type of preferential orientation, whether (110) or (200), did not change from the as-deposited films.

Upon exposure to 2% $H_2$ in argon, significant structural changes occurred, and the XRD patterns could be indexed to the brownmillerite state [16,25]. This was evidenced by the marked shift of the (110) and (200) cubic perovskite peaks to lower 2Θ angle, and the

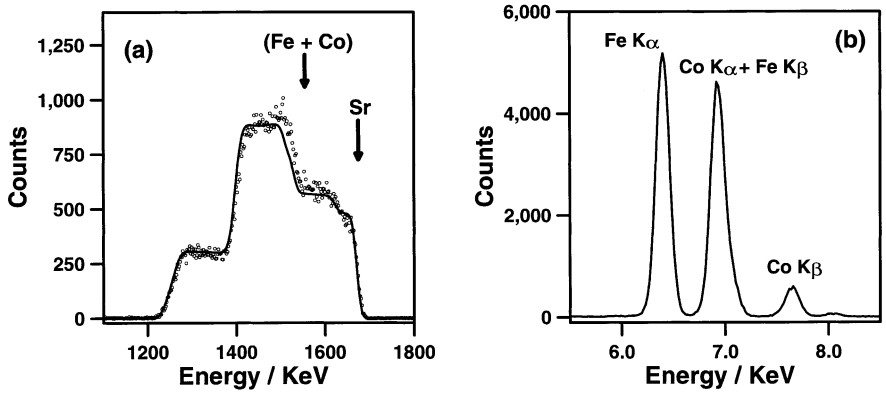


Fig. 3. (a) RBS and (b) PIXE spectra of a 300-nm $SrFe_{0.5}Co_{0.5}O_x$ film deposited on sapphire.

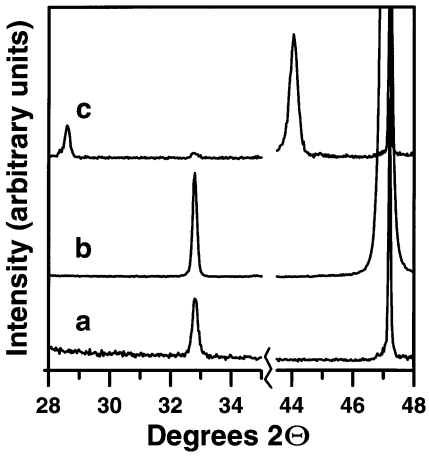


Fig. 4. XRD for films after treatment in 100% $O_2$ at 500 °C for 16 h: (a) $SrFeO_x$; (b) $SrFe_{0.50}Co_{0.50}O_x$; and (c) $SrCoO_x$. Note that there is an interference from a $CuK_\beta$ peak of the sapphire substrate at $2\Theta = 47.2°$, which overlaps with the (200) CP peak.

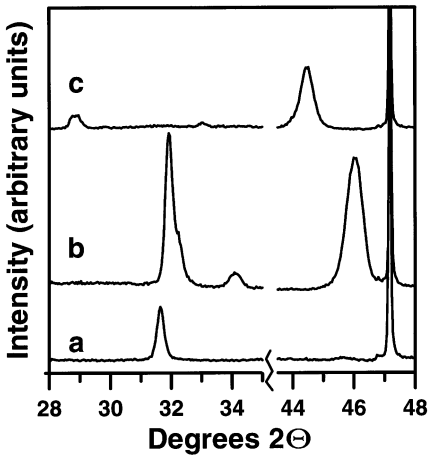


Fig. 5. XRD for films after treatment in 2% $H_2$/Ar at 500 °C for 16 h: (a) $SrFeO_x$; (b) $SrFe_{0.50}Co_{0.50}O_x$; and (c) $SrCoO_x$. The sharp peak at $2\Theta = 47.2°$ is from a $CuK_\beta$ peak of the sapphire substrate.

appearance of additional peaks consistent with a larger unit cell of lower symmetry. A striking example is the $SrFe_{0.5}Co_{0.5}O_x$ film, which shows the appearance of an intense peak at $2\Theta = 11.2°$ after the thermochemical reducing step (Fig. 6c). Similar results were obtained for both $SrFe_{0.75}Co_{0.25}O_x$ and $SrFe_{0.25}Co_{0.75}O_x$ films. The $SrFeO_x$ film also showed a weak reflection at $2\Theta = 11.2°$. These peaks are attributed to the (020) reflection of the larger brownmillerite structure [16,25].

For the $SrFe_{0.5}Co_{0.5}O_x$ film, a less intense peak at $2\Theta = 11.5°$ was observed after the thermochemical oxidation treatment (Fig. 6b). This indicates that perovskite-type supercells may form, even after thermochemical oxidizing treatments, and matches the observation that very weak reflections at $d = 14.31$, 7.7 and 5.34 Å were observed for cubic $SrFe_{0.5}Co_{0.5}O_3$ powder [26], suggesting possible transitions to lower symmetry. Indications of such expanded unit cells for $SrFeO_x$ [5,24,27] and $SrFe_{0.8}Co_{0.2}O_x$ [28,29] have previously been reported and attributed to oxygen vacancy ordering, forming, for example, $SrFeO_{2.86}$ tetragonal and $SrFeO_{2.73}$ orthorhombic perovskite-type structures [24]. Cation ordering between the Fe and Co atoms may also result in an expanded unit cell, forming an ordered double perovskite of the type that has been described for $SrFe_{0.5}Mo_{0.5}O_3$ [30].

The $SrCoO_x$ film remained preferentially (210)-oriented, and the XRD peaks shifted only slightly to a higher $2\Theta$ angle upon exposure to 2% $H_2$ in argon. In contrast to all the other films, this corresponds to a slight contraction of the unit cell. This is illustrated in Fig. 7 for the $SrFe_yCo_{1-y}O_x$ series of films, which shows the variation of the equivalent cubic unit cell parameter, $a$, derived from the (110) cubic perovskite peak or its equivalent. In all cases except for $SrCoO_x$, the unit cell parameter, $a$, increased as a result of the thermochemical reduction treatment. This difference was greatest for $SrFeO_x$, and decreased with increasing Co content in the film. This structural trend is consistent with sensor functionality observations, which showed that the iron-rich films in the $SrFe_yCo_{1-y}O_x$ series exhibited significantly greater changes in conductivity at 500 °C for the range of oxygen/nitrogen gas compositions $10^{-5} \leq p[O_2] \leq 1$ atm [4]. Moreover, this also matches the results obtained using in situ XRD (Section 3.3).

XPS measurements of the $SrFe_yCo_{1-y}O_x$ series of films after both thermochemical oxidizing and reducing conditions showed that for all films except $SrCoO_x$,

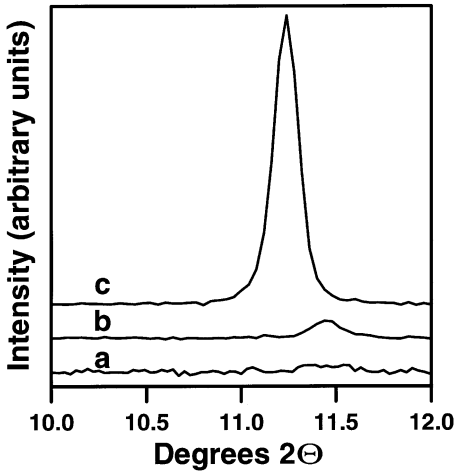


Fig. 6. XRD for $SrFe_{0.50}Co_{0.50}O_x$ films showing evolution of the high-angle reflection at $2\Theta = 11.2°$ attributable to the formation of a supercell with $d = 2a_p$ (where $a_p$ is the lattice parameter of the perovskite unit cell): (a) as-deposited film; (b) after exposure to 100% $O_2$ at 500 °C; and (c) after exposure to 2% $H_2$/Ar at 500 °C.

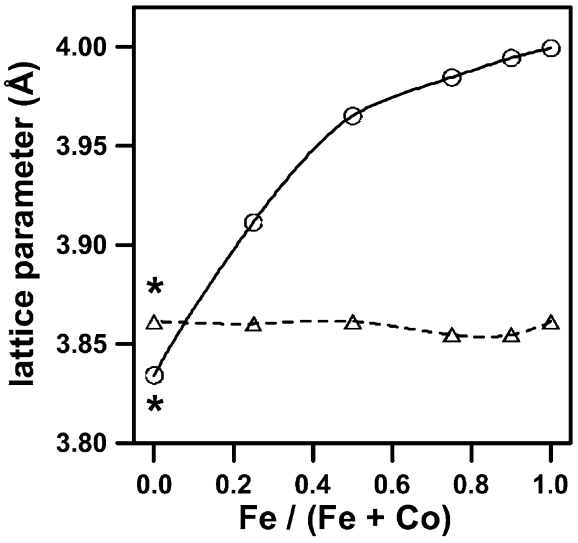


Fig. 7. Plot showing the variation of the lattice parameter, *a*, for the $SrFe_yCo_{1-y}O_x$ series of films at ambient temperature, after thermochemical treatments in 100% $O_2$ (*dashed line*) and 2% $H_2$/Ar (*solid line*) gas mixtures. The equivalent cubic lattice parameter, *a*, was derived from the (110) cubic peak or its equivalent lower symmetry peak(s) for the brownmillerite or hexagonal structure ($SrCoO_x$). *The $SrCoO_x$ perovskite phase is not stable at room temperature (see text for details).

there were only minor differences in the XPS O 1s, Sr 3d, Co 2p and Fe 2p spectra. Two peaks are observed for the O 1s XPS region (Fig. 8), one at 529.5 eV and the other at a higher binding energy between 531 and 532 eV. The higher-energy O 1s peak for perovskite surfaces is attributed to surface-bound oxygen species, possibly oxygen weakly bound on the surface, surface hydroxyls, or to a surface metal–O bond, while the lower-energy peak is attributed to lattice oxygen [6,31–38]. Moreover, the higher-binding-energy peaks were much more sensitive to $Ar^+$ etching treatment than the lower-energy peak, thus supporting this assignment.

The Sr 3d XPS region (Fig. 9) shows a doublet, $3d_{5/2}$ and $3d_{3/2}$, at 133 and 135 eV, respectively. These assignments are consistent with the chemical shifts reported for other similar Sr-containing perovskites [32–34,36]. Although no curve fitting was performed, these doublets are likely comprised of more than one contribution, assigned to Sr present in the bulk and at surface sites as SrO and $SrCO_3$ [32].

Both the Fe 2p and Co 2p spectral regions show at least one set of doublets between 700 and 735, and 770 and 810 eV, respectively. These showed small spectral changes after different thermochemical treatments, but were difficult to interpret due to the closeness of peaks associated with different oxidation states of iron and cobalt, and the presence of satellite shake-up lines associated with the paramagnetic Fe(III) and Co(III) states [39].

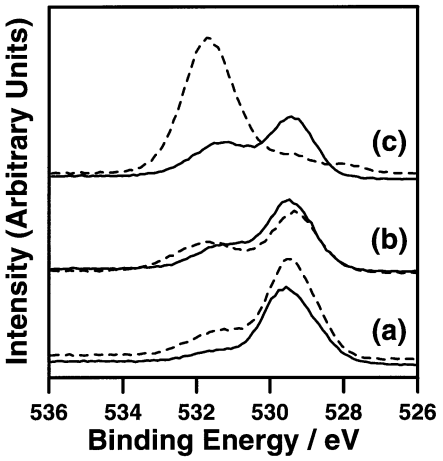


Fig. 8. High-resolution O 1s XPS spectra for: (a) $SrFeO_x$; (b) $SrFe_{0.50}Co_{0.50}O_x$; and (c) $SrCoO_x$ after thermochemical treatments at 500 °C in 100% $O_2$ (*solid lines*) and 2% $H_2$/Ar (*dashed lines*). A 15-s $Ar^+$ sputter etch was used to pre-clean the surface.

The thermochemical reducing treatment of $SrCoO_x$, in contrast to the other films, caused surface changes resulting in notably different XPS spectra (Fig. 8c, Fig. 9c, Fig. 10b). It is proposed that prolonged exposure to the reducing gas mixture of 2% $H_2$ in argon at 500 °C resulted in decomposition of the surface of the film to form SrO. SrO then reacted with $CO_2$ from the ambient air to form $SrCO_3$ This type of behavior has been reported for $La_{0.3}Sr_{0.7}CoO_x$ (LSCO) perovskite membranes during oxygen permeation experiments [31]. In this case, a 10–15-nm surface SrO layer was formed by reduction of the $La_{0.3}Sr_{0.7}CoO_x$ phase following prolonged exposure to a 1.4% $O_2$ in helium gas mixture at 900 °C. After cooling and exposure to the atmosphere,

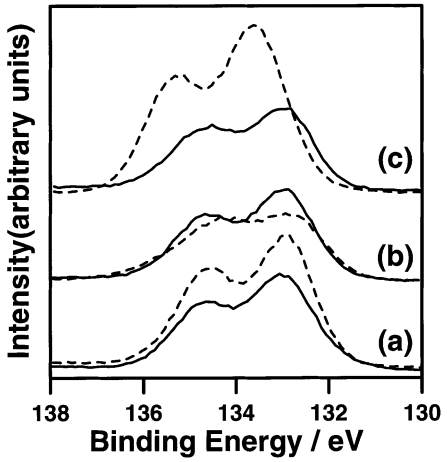


Fig. 9. High-resolution Sr 3d XPS spectra of: (a) $SrFeO_x$; (b) $SrFe_{0.50}Co_{0.50}O_x$; and (c) $SrCoO_x$ after thermochemical treatments at 500 °C in 100% $O_2$ (*solid lines*) and 2% $H_2$/Ar (*dashed lines*). A 15-s $Ar^+$ sputter etch was used to pre-clean the surface.

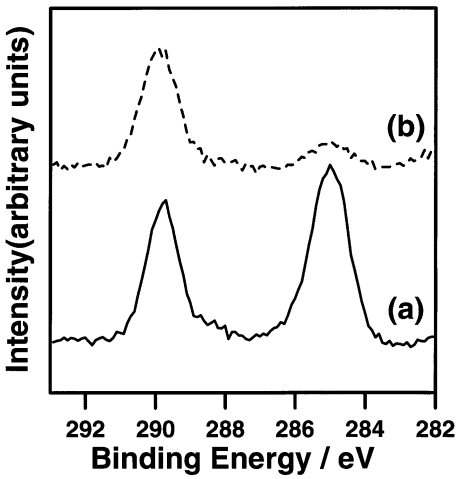


Fig. 10. C 1s XPS spectra for $SrCoO_x$ after thermochemical treatment at 500 °C in 2% $H_2$/Ar (a) before and (b) after a 30-s $Ar^+$ etch.

$CO_2$ reacted with SrO to form $SrCO_3$, which was identified by XPS.

Evidence for this is also supported by the XPS O 1s, Sr 3d and C 1s spectral regions. For the $SrCoO_x$ film, an intense higher-binding-energy O 1s peak is observed at 531.7 eV (Fig. 8c) after the thermochemical reducing treatment. This chemical shift is consistent with that expected for a carbonate oxygen [32,39]. The intensity of the lower-energy 529.5-eV peak is much smaller than for the film treated under oxidizing conditions, indicating that the dominant surface oxygen species is no longer the lattice oxygen associated with the perovskite phase. The Sr 3d doublet (Fig. 9c) also showed a shift to higher binding energy with the Sr $3d_{5/2}$ peak located at 133.6 eV, which approaches the 133.2-eV value reported for $SrCO_3$ [39]. Furthermore, a high-energy C 1s XPS peak at 290 eV (Fig. 10) also matches the 289.5-eV peak reported for $SrCO_3$ [39]. A 30-s $Ar^+$ surface etch causes the amorphous carbon peak at 285.0 eV, which is associated with carbonaceous surface contamination, to decrease in intensity. In contrast, the intensity of the carbonate peak at 290 eV is almost unaffected. The surface $CO_3^{2-}$ XPS peak assignments for the O 1s, C 1s and Sr 3d spectral regions are similar to those made for a series of $La_{1-x}Sr_x$-based perovskite-type oxides [32]. These observations indicate that the $SrCoO_x$ film has undergone substantial surface decomposition to form a carbonate species after exposure to ambient atmosphere.

When the relative surface stoichiometry values for the $SrFe_yCo_{1-y}O_x$ series of films obtained from XPS are plotted, a number of trends are apparent (Fig. 11). First of all, the surface of all films appear to be enriched in strontium, compared to their bulk stoichiometry (Table 1). This may be the result of the formation of a surface segregated phase, which has been described elsewhere for the perovskite interface [20–22,31,33,38,40,41]. However, it is noted that calibrated reference samples were not used for the determination of the surface stoichiometry of these films by XPS. The strontium enrichment of the surface contrasts with the surface metal enrichment observed for the as-deposited $SrFe_{0.5}Co_{0.5}O_x$ film by RBS (Section 3.1). This is probably a consequence of the post-deposition thermochemical treatments, which may change the relative metal concentrations at the surface [20–22,31,33,38,40,41].

The Co and Fe stoichiometry changes as expected across the $SrFe_yCo_{1-y}O_x$ series of films except for the $SrCoO_x$ film after thermochemical reduction (Fig. 11b). This film showed much lower than expected Co content, resulting from the formation of a strontium-enriched carbonate phase at the surface. Moreover, the carbon content for this film was anomalously high, consistent with the presence of such a carbonate phase.

FEG-SEM images of the $SrCoO_x$ films after oxidizing and reducing thermochemical treatments show marked

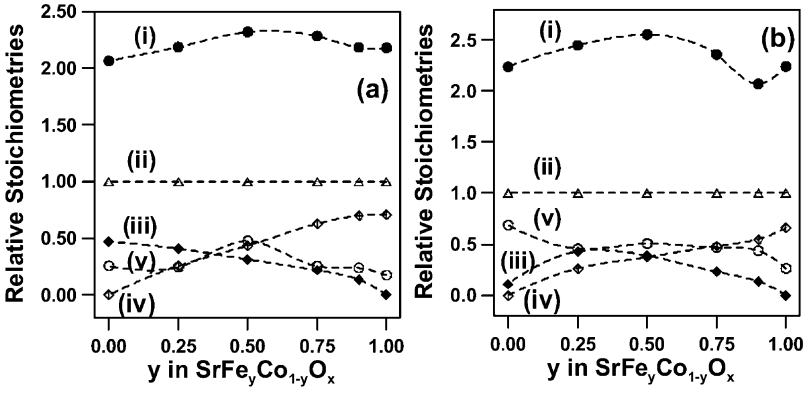


Fig. 11. Plot showing the relative surface stoichiometries of the $SrFe_yCo_{1-y}O_x$ series of films after thermochemical treatments at 500 °C in (a) 100% $O_2$ and (b) 2% $H_2$/Ar gas mixtures: (i) ● oxygen; (ii) Δ strontium; (iii) ◇ iron; (iv) ◆ cobalt; and (v) ○ carbon. A 15-s $Ar^+$ sputter etch was used to pre-clean the surface prior to chemical analysis by XPS.

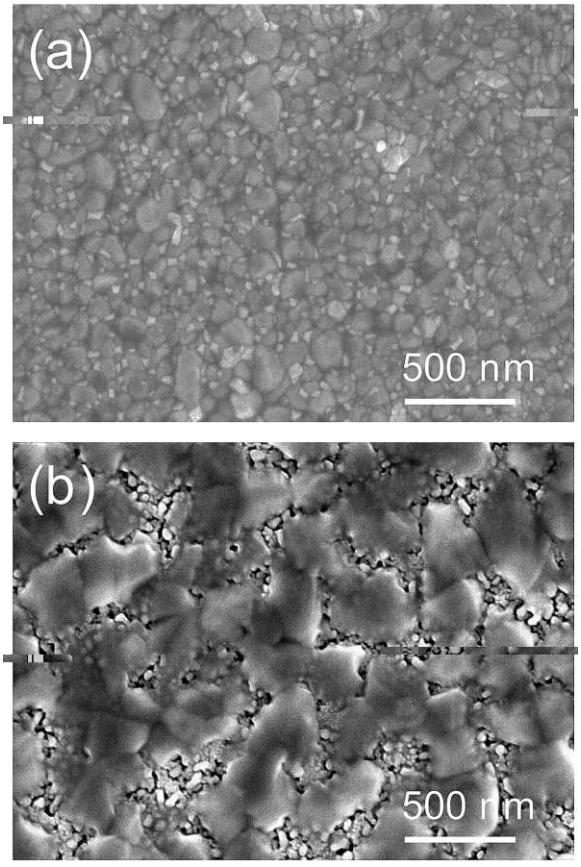


Fig. 12. SEM images of the $SrCoO_x$ film after thermochemical treatments at 500 °C in (a) 100% $O_2$ and (b) 2% $H_2$/Ar gas mixtures.

changes in the morphology of the films (Fig. 12). The $SrCoO_x$ film exposed to oxygen gas at 500 °C showed a polycrystalline film with grain size dimensions ranging between 20 and 150 nm. After the thermochemical reducing treatment, substantial grain growth occurred, with large grains between 250 and 500 nm appearing. Smaller grains 100 nm were found between and under these larger grains. The two different grain types suggest that film decomposition has occurred, with two separate phases being present.

### 3.3. In situ XRD study of films

The chemical sensitivity of the $SrFe_yCo_{1-y}O_x$ films is due in large part to the reversible physical and structural changes that occur at elevated temperatures ( 250 °C) when the films are exposed to different gas mixtures [4]. Accordingly, the structural changes in the $SrFe_yCo_{1-y}O_x$ series of films upon changing gas composition from air to nitrogen were examined in situ at 500 °C by XRD. The temperature of 500 °C was selected as a typical operation temperature for this sensor material.

All films except $SrCoO_x$ showed evidence of unit cell expansion upon changing from air to nitrogen exposure (Fig. 13, Table 2). This effect was most pronounced for the $SrFe_{0.75}Co_{0.25}O_x$ and $SrFe_{0.5}Co_{0.5}O_x$ films and could best be observed by examining the changes in the (110) and (200) cubic or slightly distorted tetragonal perovskite peaks near $2\Theta = 32°$ and 46°, respectively. The shift towards lower $2\Theta$ angles for these peaks and the appearance of additional peaks, some of which were as low as $2\Theta = 11.2°$, were all consistent with the transformation in structure from a cubic perovskite to brownmillerite with ordered oxygen vacancies [4,5,24,27].

In contrast, changing from air to nitrogen exposure caused slight shifts of the XRD peaks towards higher $2\Theta$ angles for the $SrCoO_x$ film. This is consistent with the decrease in lattice parameters observed for this film after the more severe thermochemical reducing treatment (Section 3.2).

The lattice parameters for the films exposed to the two gas mixtures (Table 2) indicated that a phase change from tetragonal perovskite (TP) to brownmillerite (BM) occurred for $SrFeO_x$, $SrFe_{0.75}Co_{0.25}O_x$ and $SrFe_{0.5}Co_{0.5}O_x$. The TP phase was observed for the films exposed to air, whereas the BM phase was observed for the films exposed to nitrogen. The TP phase, which is a distortion of the higher-symmetry CP phase, was found to provide better XRD refinements compared to the CP phase, although the film is probably an equilibrium mixture of both the CP and TP phases. The TP phase has previously been shown to exist in equilibrium with the CP phase for the bulk $SrFeO_x$ system at temperatures

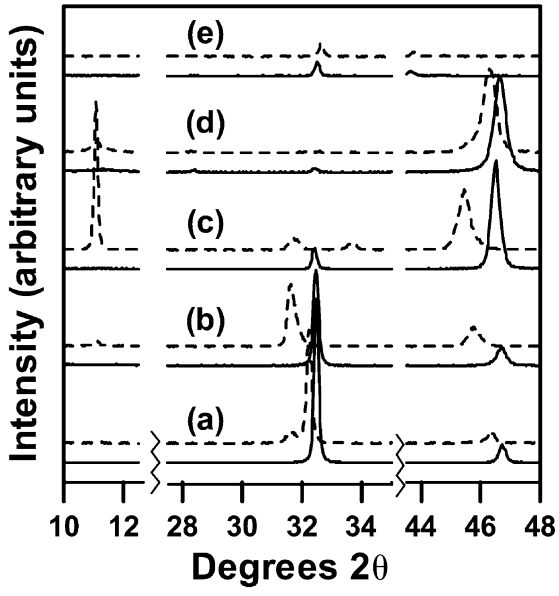


Fig. 13. XRD patterns of: (a) $SrFeO_x$; (b) $SrFe_{0.75}Co_{0.25}O_x$; (c) $SrFe_{0.50}Co_{0.50}O_x$; (d) $SrFe_{0.25}Co_{0.75}O_x$; and (e) $SrCoO_x$ films taken in situ at 500 °C in UHP $N_2$ (*upper dashed lines*) and air (*bottom dark lines*).

Table 2
Reversible structural changes occurring in situ at 500 °C, as determined by XRD, for the $SrFe_yCo_{1-y}O_x$ series of films resulting from changes in gas composition

| Composition | Gas | Unit cell | Lattice parameters (Å) | | | Normalized unit cell volume (Å$^3$) |
|---|---|---|---|---|---|---|
| | | | *a* | *b* | *c* | |
| $SrFeO_x$ | Air | TP | 3.889 (4) | | 3.908 (2) | 59.11 (10) |
| $SrFeO_x$ | $N_2$ | BM[a] | 5.657 (2) | 5.622 (2) | 5.525 (3) | 61.03 (4) |
| $SrFe_{0.75}Co_{0.25}O_x$ | Air | TP | 3.8870 (7) | | 3.9063 (9) | 59.02 (2) |
| $SrFe_{0.75}Co_{0.25}O_x$ | $N_2$ | BM | 5.660 (2) | 15.926 (7) | 5.563 (3) | 62.68 (5) |
| $SrFe_{0.5}Co_{0.5}O_x$ | Air | TP | 3.9030 (2) | | 3.9146 (4) | 59.63 (1) |
| $SrFe_{0.5}Co_{0.5}O_x$ | $N_2$ | BM | 5.678 (4) | 15.937 (8) | 5.640 (3) | 63.79 (6) |
| $SrFe_{0.25}Co_{0.75}O_x$ | Air | BM[b] | 5.636 (3) | 15.581 (7) | 5.523 (3) | 60.63 (6) |
| $SrFe_{0.25}Co_{0.75}O_x$ | $N_2$ | BM[b] | 5.652 (4) | 15.64 (1) | 5.501 (4) | 60.80 (8) |
| $SrCoO_x$ | Air | OR[c] | 2.9804 (8) | 3.0079 (10) | 14.298 (6) | 64.09 (4) |
| $SrCoO_x$ | $N_2$ | OR[c] | 2.9700 (9) | 3.0054 (9) | 14.241 (7) | 63.56 (5) |

TP, tetragonal perovskite lattice; BM, brownmillerite lattice; OR, orthorhombic lattice.
[a] Film is likely a mixture of brownmillerite and tetragonal perovskite phases.
[b] Film is a mixture of brownmillerite and rhombohedral phases
[c] Refinements using the hexagonal [17] and rhombohedral [42] cells showed larger residual errors than those based on the OR structure.

lower than 500 °C for oxygen stoichiometry 2.86 $x$ 2.97 [5,24]. Two-phase regions containing both cubic perovskite and brownmillerite for bulk powders have been reported for both the $SrFeO_x$ [24,27] and $SrFe_{0.8}Co_{0.2}O_x$ [28] systems. According to the phase diagrams reported for these systems, this two-phase region exists over large ranges of oxygen stoichiometry at 500 °C. For $SrFeO_x$ at 500 °C this region is bounded by 2.56 $x$ 2.66 and corresponds to an equilibrium gas composition of $p[O_2]=10^{-4}$ atm. For $SrFe_{0.8}Co_{0.2}O_x$ it is necessary to extrapolate the temperature to 500 °C, since the phase diagram is only given from 550 to 900 °C. When this was carried out, the two-phase region was estimated to occur in the range 2.49 $x$ 2.63 and corresponds to an oxygen partial pressure slightly less than 0.2 atm. The presence of these perovskite–brownmillerite two-phase regions has been shown to be associated with enhanced oxygen gas sensitivity [4,23].

The $SrFe_{0.25}Co_{0.75}O_x$ film was indexed to the BM phase for both air and nitrogen exposure, despite the uncertainty due to the presence of trace amounts of a $SrCoO_x$-type rhombohedral phase [42], identified by a weak reflection at $2\Theta=28.3°$. The presence of the brownmillerite phase for both air and nitrogen exposure at 500 °C can be explained on the basis of the high-temperature phase diagram published for $SrFe_{0.8}Co_{0.2}O_x$ [28], which indicates that equilibration in air at 500 °C should favor the brownmillerite structure. As a result, no phase change was detected. Likewise, the $SrCoO_x$ film was indexed to an orthorhombic unit cell for both gas exposures with no phase transitions occurring.

Films that exhibited TP → BM phase transformations also showed larger changes in the normalized unit cell volume [unit cell volume per $Sr(Fe,Co)O_x$ formula unit]. For example, $SrFe_{0.5}Co_{0.5}O_x$ showed a 7.0% unit cell volume expansion as a result of changing the gas composition from air to nitrogen. In contrast, $SrFe_{0.25}Co_{0.75}O_x$ showed only a 0.3% expansion of the equivalent unit cell volume upon changing from air to nitrogen, and $SrCoO_x$ actually showed a 0.8% contraction. However, the $SrCoO_x$ system is complicated by the instability of the 1:1 perovskite composition, which forms $Sr_6Co_5O_{15}$ and $Co_3O_4$ in air upon cooling [19].

## 4. Conclusions

Non-stoichiometric $SrFe_yCo_{1-y}O_x$ films of different composition can be prepared by pulsed laser deposition on sapphire substrates. The as-deposited polycrystalline films were indexed to either the cubic perovskite ($SrFe_yCo_{1-y}O_x$; $y=1.0$, 0.9, 0.75, 0.5 and 0.25) or hexagonal ($SrCoO_x$) phases, and were all found to exhibit some degree of preferential orientation. Elemental analyses by both RBS/PIXE and ICP-AES were consistent and indicated a slight (Co + Fe) enrichment for some of the films.

Thermochemical treatments at 500 °C in both oxidizing (100% $O_2$) and reducing (2% $H_2$ in Ar) gas mixtures showed all the films except $SrCoO_x$ were stable under these conditions, despite undergoing significant reversible structural changes resulting from the changing oxygen stoichiometry in the films. Surface decomposition of the $SrCoO_x$ film to form a Sr-enriched carbonate layer was confirmed by XPS and SEM analysis.

In situ XRD measurements under conditions expected for sensor operation, performed on the films at 500 °C, confirmed that reversible structural changes occurred in

the $SrFe_yCo_{1-y}O_x$ series of films upon changing gas composition from air to nitrogen. This structural variability is important, since it forms the basis for bulk oxygen chemical sensors exhibiting high sensitivity.

## Acknowledgments

The authors would like to thank G. Pleizier for the XPS and SEM analysis, J. Fraser for FEG-SEM analysis, V. Boyko for ICP-AES analysis, and Dr W. Lennard and Dr Joon Kon Kim at the University of Western Ontario Surface Science Facility for the RBS and PIXE analysis.

## References

[1] Y. Teraoka, H.M. Zhang, S. Furukawa, N. Yamazoe, Chem. Lett. 1985 (1985) 1743.
[2] Y. Teraoka, H.M. Zhang, K. Okamoto, N. Yamazoe, Mater. Res. Bull. 23 (1988) 51.
[3] V.V. Kharton, E.N. Naumovitch, A.V. Nikolaev, J. Membrane Sci. 111 (1996) 149.
[4] J.J. Tunney, M.L. Post, X. Du, D. Yang, J. Electrochem. Soc. 149 (2002) H113.
[5] M.L. Post, B.W. Sanders, P. Kennepohl, Sensors Actuators B 13/14 (1993) 272.
[6] Y. Yu, Y.F. Chen, Z.G. Liu, L. Sun, S.B. Xiong, N.B. Ming, Z.M. Ji, J. Zhou, Appl. Phys. A: Mater. Sci. Process. 64 (1997) 69.
[7] H. Tanaka, N. Matsuoka, S. Oki, S. Gohda, T. Kawai, Thin Solid Films 326 (1998) 51.
[8] X. Chen, N.J. Wu, D.L. Ritums, A. Ignatiev, Thin Solid Films 342 (1999) 61.
[9] D. Waller, L.G. Coccia, J.A. Kilner, I.W. Boyd, Solid-State Ionics 134 (2000) 119.
[10] C. Zhang, H. Deng, J. Varon, B. Abeles, Y. Yang, A.Q. Pham, A.J. Jacobson, in: G.-A. Nazri, J.-M. Tarascon, M. Schreiber (Eds.), Solid-State Ionics IV, Boston, USA, 28 November–1 December 1994, Mater. Res. Soc. Symp. Proc. 369 (1995) 401.
[11] W.N. Lennard, C.P. McNorgan, Quantitative Analysis of Rutherford Kinematics Simulation Software, University of Western Ontario, Interface Science Western, London, ON, Canada (2001).
[12] M. Schuster, H. Göbel, J. Phys. D: Appl. Phys. 28 (1995) A270.
[13] G.S. Pawley, J. Appl. Crystallogr. 14 (1981) 357.
[14] Bruker AXS, TOPAS V2.0: General Profile and Structure Analysis Software for Powder Diffraction Data, User Manual, Bruker AXS, Karlsruhe, Germany, 2000.
[15] Powder Diffraction File, Card 40-0905, Joint Committee on Powder Diffraction Standards, ASTM, Philadelphia, PA, 1967.
[16] Powder Diffraction File, Card 17-0932, Joint Committee on Powder Diffraction Standards, International Center for Diffraction Data, Newton Square, PA, 1997.
[17] Powder Diffraction File, Card 40-1018, Joint Committee on Powder Diffraction Standards, International Center for Diffraction Data, Newton Square, PA, 1997.
[18] J. Rodriguez, J.M. Gonzalez-Calbet, Mater. Res. Bull. 21 (1986) 429.
[19] W.T.A. Harrison, S.L. Hegwood, A.J. Jacobson, Chem. Commun. 1995 (1995) 1953–1954.
[20] G. Horvath, J. Gerblinger, H. Meixner, J. Giber, Sensors Actuators B 32 (1996) 93.
[21] S.B. Desu, D.A. Payne, J. Am. Ceram. Soc. 73 (1990) 3391.
[22] S.B. Desu, D.A. Payne, J. Am. Ceram. Soc. 73 (1990) 3398.
[23] J.J. Tunney, M.L. Post, J. Electroceram. 5 (2000) 63–69.
[24] Y. Takeda, K. Kanno, T. Takada, O. Yamamoto, M. Takano, N. Nakayama, Y. Bando, J. Solid-State Chem. 63 (1986) 237.
[25] Powder Diffraction File, Card 30-0226, Joint Committee on Powder Diffraction Standards, International Center for Diffraction Data, Newton Square, PA, 1997.
[26] Powder Diffraction File, Card 46-0335, Joint Committee on Powder Diffraction Standards, International Center for Diffraction Data, Newton Square, PA, 1997.
[27] J. Mizusaki, M. Okayasu, S. Yamauchi, K. Fueki, J. Solid State Chem. 99 (1992) 166.
[28] L.M. Liu, T.H. Lee, L. Qiu, Y.L. Yang, A.J. Jacobson, Mater. Res. Bull. 31 (1996) 29.
[29] L. Qiu, T.H. Lee, L.M. Liu, Y.L. Yang, A.J. Jacobson, Solid-State Ionics 76 (1995) 321.
[30] F.S. Galasso, Structure, Properties and Preparation of Perovskite-Type Compounds, Pergamon, London, 1969.
[31] R.H.E. van Doorn, H.J.M. Bouwmeester, A.J. Burggraaf, Solid-State Ionics 111 (1998) 263.
[32] P.A.W. van der Heide, Surf. Interface Anal. 33 (2002) 414.
[33] P.A.W. van der Heide, Surf. Sci. 473 (2001) 59.
[34] M. Machkova, N. Brashkova, P. Ivanov, J.B. Carda, V. Kozhukharov, Appl. Surf. Sci. 119 (1997) 127.
[35] N. Gunasekaran, S. Rajadurai, J.J. Carberry, N. Bakshi, C.B. Alcock, Solid-State Ionics 73 (1994) 289.
[36] A.E. Bouquet, P. Chalker, J.F. Dobson, P.C. Healy, S. Myhra, J.G. Thompson, Physica C 160 (1989) 252.
[37] K. Tabata, I. Matsumoto, S. Kohiki, J. Mater. Sci. 22 (1987) 1882.
[38] J.A. Marcos, R.H. Buitrago, E.A. Lombardo, J. Catal. 105 (1987) 95.
[39] J.F. Moulder, W.F. Stickle, P.E. Sobol, K.D. Bomben, Handbook of X-Ray Photoelectron Spectroscopy, Perkin Elmer Corporation, Physical Electronics Division, Eden Prairie, Minnesota, 1992.
[40]